



www.chemasianj.org



Exploring Carbonyl Chemistry in Non-aqueous Mg Flow Batteries

Yunan Qin^{+,[a]} Kathryn Holguin^{+,[b]} Dillon Fehlau,^[a] Chao Luo,^{*[b, c]} and Tao Gao^{*[a]}

Abstract: Non-aqueous redox flow batteries (RFBs) are emerging electrochemical technologies for grid energy storage. Non-aqueous Mg RFBs that use Mg metal as the anode are especially promising due to various benefits of the Mg metal anode, including its low potential, high volumetric capacity, SEI-free, highly reversible operation and low cost. Despite the potential, there are rarely any studies on developing non-aqueous Mg RFBs. Herein, a non-aqueous Mg redox flow battery using a polymer catholyte is reported. Through rational molecular engineering, a carbonyl-based moiety is combined with a polyethylene glycol moiety to achieve a polymer with high voltage and high solubility in the ether-based electrolyte. A series of polymers with different polyethylene glycol chain lengths are synthesized and

their performances are measured first at the molecular level, and then at the device level in a Mg redox flow battery using a Mg foil as the anode, the polymer solution as the catholyte and a porous membrane as the separator. The flow battery delivers a voltage of 1.8 V, a maximum capacity of 475 mAh/L, an average Coulombic efficiency of 90.5%, an average voltage efficiency of 67.4%, an energy efficiency of 61.0%, and an energy density of 0.855 Wh/L. Systematic mechanistic studies are performed to understand the performance decay mechanism and possible strategies for future improvement are discussed. This work opens a new avenue for the development of energy storage technologies for grid electricity storage.

Introduction

Decarbonizing electricity generation requires mass deployment of renewable energy sources like solar and wind power. To bridge the intermittent electricity generation of these renewable sources with our demand for reliable and continuous electricity, large-scale energy storage is necessary. Among various energy storage technologies, redox flow batteries (RFBs) are promising due to their high-energy efficiency, great design flexibility, and good scalability. Since the debut of RFBs in the 1970s, a rich variety of RFBs have been developed, among which the all-vanadium and Zn/bromine RFBs are the most successful. However, their high-cost and toxic materials remain problematic. Designing new RFBs based on sustainable, low-cost, safe and abundant materials is critical to enable the mass adoption of RFBs for grid energy storage.

In the past decade, aqueous RFBs with organic catholytes/ anolytes attract the most attention due to the abundant raw

- [a] Y. Qin, D. Fehlau, T. Gao Department of Chemical Engineering University of Utah Salt Lake City, UT (USA) E-mail: taogao@chemeng.utah.edu
- [b] K. Holguin, C. Luo Department of Chemistry and Biochemistry George Mason University Fairfax, VA-22030 (USA) E-mail: cluo@amu.edu
- [c] C. Luo Quantum Science & Engineering Center George Mason University Fairfax, VA-22030 (USA)
- [⁺] These authors contribute equally.
 - Supporting information for this article is available on the WWW under https://doi.org/10.1002/asia.202200587

This manuscript is part of a special collection on Redox Flow Batteries.

material and high structural tunability of organic materials. [1,2,3] However, electrolysis of water limits the voltage of these RFBs (typically < 1.5 V) therefore curtails their energy density. [2] To circumvent this challenge, non-aqueous RFBs have emerged as promising alternatives due to the much larger voltage window of organic electrolytes (up to 6 V).[4] In addition, the wide liquid range of organic solvents enables non-aqueous RFBs capable of operating in extreme temperatures.^[5] A large variety of organic and inorganic materials have been developed for non-aqueous RFB.[5-17] Nevertheless, a lack of low potential anode materials limits its voltage to 2.5 V.[18] As alternatives, non-aqueous hybrid RFBs with Li/Na metal anodes are able to fully utilize the high voltage potential of organic electrolytes due to the very low potentials of these alkali metals.[19] However, an Li/Na-ion conducting membrane is mandatory to separate the organic electrolytes from the very reactive alkali metal, which increases the overall cost and limits their performance. [20,21]

With slightly higher potential than Li and Na, Mg metal has been proved to be thermodynamically stable in some organic electrolytes, [22] making it a promising anode material for nonaqueous hybrid RFBs. Such novel RFBs based on the Mg anode have several unique advantages: 1) low material cost. Mg is a major industrial metal and abundant in earth (abundance similar as iron, sodium, manganese). Mg electrolytes can be made from abundant salts such as MgCl₂ and industrial solvents such as glyme. Potential corrosion concern of the chloride is solvable by leveraging the experience of the commercialized Zn/bromine battery. 2) high voltage and energy density. Mg has the lowest potential among all industrial metals. An RFB with a Mg metal anode can provide a voltage of 3-4 V. In addition, Mg metal is denser than Li, offering twice the energy storage capability at the same volume. Together with a high-capacity cathode, a high-energy-density Mg RFB can be achieved. 3) the highly reversible and stable anode. Reversible Mg deposition/





striping for up to 2500 cycles has been demonstrated in rechargeable Mg batteries,^[22] promising long cycle life for RFBs based on the Mg metal anode.

Despite the great promise, there are barely any report on Mg hybrid RFBs. Following our companion Letter^[23] that reported the first Mg hybrid flow battery with a polymer catholyte, in this research article, we systematically study how the functional group of the polymer catholytes (Figure 1) affects the flow battery performance at both the molecular level and the device level. Specifically, the repeating unit of the polymers consists of a carbonyl group as the redox-active moiety and a polyethylene glycol chain as the supporting moiety. By tuning the length of the supporting moiety, the solubility, the redox potential and kinetics, as well as the electrochemical performances of the polymers in the Mg flow battery are systematically investigated. The knowledge gained in this study will provide valuable insights for designing and optimizing soluble polymer materials for high-performance Mg hybrid flow batteries in the future.

Methods

Materials

 $\rm MgCl_2$ (99.99%), Mg powder (50 mesh, > 99%), 1,4,5,8-Naphthalenetetracarboxylic dianhydride (NTCDA), Dimethylformamide (DMF), and dimethoxyethane (DME, 99.5%) were purchased from Sigma-Aldrich. LiTFSI (99.5%) was purchased from Gotion Inc. NH2-PEG3-NH2, NH2-PEG5-NH2, NH2-PEG7-NH2, NH2-PEG9-NH2, and NH2-PEG11-NH2 were purchased from Biopharma PEG Scientific, Inc. LiTFSI was dried under vacuum for 24 hours at 150 °C prior to use. DME was dried overnight by 3 Å molecular sieves before use.

Synthesis/Preparation of PIPEG Polymer Material

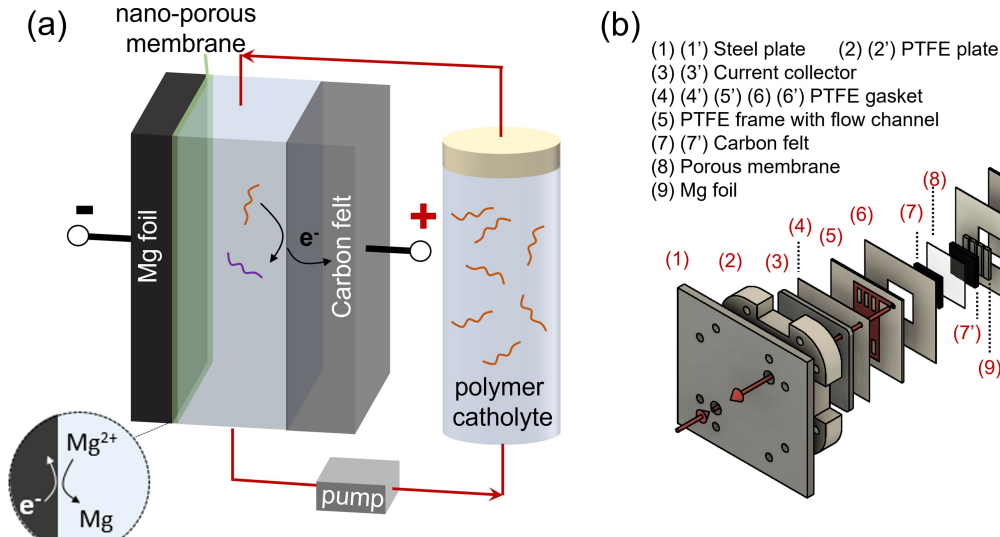
The polymer (P11) was prepared as follows: NTCDA was mixed with DMF under $\rm N_2$ gas. The solution was stirred and heated to 140 °C until completely dissolved. NH2-PEG11-NH2 was dissolved in DMF and added to the reaction solution via syringe. The reaction bath was stirred and refluxed continuously for 3 days at 140 °C. The desired polymer was isolated via simple distillation under vacuum. The resulted solid was washed with distilled water and dried in the vacuum oven at 90 °C overnight. The isolated product is a dark amber solid. The other polymers (P3, P5, P7, and P9) were synthesized by the same method.

Materials Characterization

The synthesized polymers were analyzed spectroscopically using Fourier transform infrared spectroscopy (FTIR, Nicolet iS50 FTIR Spectrometer), and X-ray diffraction (XRD, Rigaku MiniFlex using CuK α radiation) and Nuclear magnetic resonance (NMR, Bruker Ascend 400).

The polymers (P7, P9, and P11) permeability through the porous membranes was determined using a two-compartment glass diffusion cell. One compartment was filled with 15 mL polymer solution with known concentration dissolved in DME, and the other was filled with 15 mL pure DME. The tested membrane acted as the separator. The initially polymer-free solution was periodically sampled, and polymer content was determined by UV-vis (Hitachi U4100) using a pre-determined calibration curve. Permeability of polymers through the membrane was expressed by the fraction of polymer crossing the membrane per day.

SEM image and EDS analysis were collected with an FEI Quanta 600 FEG. Before analysis, samples were washed with DME solvent and dried under vacuum.



* The red line represents the flow of catholyte.

(5')

Figure 1. (a) the schematic of a Mg hybrid flow battery. (b) the design of the Mg hybrid flow battery (Inset: a picture of Mg hybrid flow battery).





Electrochemistry

Electrolyte solutions were prepared in a N_2 (99.999%) filled glove box as follows: 0.5 M of LiTFSI, 0.25 M Mg powder and 0.5 M of MgCl₂ were added to DME and the mixture was stirred for 6 hours at 45 °C, then the solutions were filtered.

Cyclic voltammogram (CV) was collected with an Interface 1010 electrochemical workstation from Gamry instruments. To collect the CV of the electrolyte, a glass carbon disk (diameter: 3 mm), a Pt wire, and a polished Mg foil were used as the working electrode, the counter electrode, and the reference electrode, respectively. To collect the CV of the polymer catholyte, a glass carbon disk or carbon felt (specific surface area: $1.50 \text{ m}^2/\text{g}$) was used as the working electrode and two polished Mg foils were used as the counter electrode and the reference electrode respectively. The diffusion coefficient D_0 and heterogeneous reduction rate constants k^0 for polymers (P7, P9, and P11) were calculated from cyclic voltammetry data at different scan rates, according to the reported method. [24]

Galvanostatic discharge-charge measurements were performed on a multi-channel battery tester made by Landt Instruments. The cell was assembled in an N2-filled glovebox as shown in Figure 1b. Cu plates were used as the current collectors. A graphite felt (area is 3 cm×3 cm, thickness is 3.42 mm) and a Mg foil were used as the cathode and the anode separated by a porous membrane (pore size: 0.034 µm, Shenzhen Jialiye Technology Co., Ltd). A graphite felt was used to support the Mg foil against the porous membrane in the anode chamber. The battery was galvanostatically charged and discharged at a current density of 50 μA cm⁻² at room temperature. The cut-off voltage for charge and discharge were set to 2.8 V and 0.8 V, respectively. In a typical test, the volume of the catholyte is 10 mL. A Master Flex L/S pump with PTFE pump head was used to pump the electrolyte. The flow rate was 5 mL/min. To test the stability of the discharged polymers (the reduced state), the cell was discharged to 0.8 V, and then put into rest with no pumping for 12 hours. After that, the cell was restarted, and the charge/discharge cycling was resumed.

Results and Discussions

Material preparation and characterization

The synthesized polymers consist of a redox-active moiety based on carbonyl groups and a solubility-tunable moiety

based on the polyethylene glycol (PEG) chain. The carbonyl groups connected by the conjugation structure function as redox-active sites to reversibly react with electrons/cations in the Mg RFBs, while the length of the PEG chain is adjustable to tune the solubility of the polymer in organic electrolytes. The polymers are named as P3, P5, P7, P9, and P11 according to the length of the PEG chain in the repeating unit of each polymer (Scheme 1). The structure was characterized by Fourier-transform infrared (FTIR) spectroscopy, X-ray diffraction (XRD), proton nuclear magnetic resonance (1H NMR), and carbon-13 nuclear magnetic resonance (13C NMR). The FTIR spectrum (Figure S1a) of the precursor, NTCDA (black), shows a peak at 3084 cm⁻¹, corresponding to the =C–H stretching vibrations from benzene rings, while the peak at 1761 cm⁻¹ corresponds to the vibrations of the carbonyl groups. The peak at 1028 cm⁻¹ corresponds to the vibrations of the C-O-C bonds in the anhydride ring. In contrast, the FTIR spectra of the polymers P3, P5, P7, P9, and P11, shows that as the chain length increases, the peak at 2860 cm⁻¹ intensifies and broadens, this is attributed to overlapping signals from the =C-H vibrational stretching of the benzene ring and the C-N-C vibrational stretching of the polymer. The newly formed C-N-C bond of the polymer is further confirmed by the vibrational peaks at 1330 cm⁻¹, presenting in the FTIR spectra of each polymer. The peaks at 1704 cm⁻¹ and 1662 cm⁻¹ correspond to the symmetrical and asymmetrical vibrations of the carbonyl groups, respectively, while the broadening peak (with increasing chain length) at 1090 cm⁻¹ corresponds to the vibrational stretching of the ether groups in PEG chain (C-O-C). The crystal structures of NTCDA and the polymers were studied by XRD as shown in Figure S1b. Though NTCDA shows a crystal structure with several sharp XRD peaks from 10 to 30 degree, the synthesized polymers are amorphous without any obvious XRD peaks. The molecular structure of each polymer was further confirmed by NMR. The ¹H NMR spectrum (Figure S2a) of the starting material, NTCDA shows one peak at 8.708 ppm, representing the protons in the benzene ring structure of NTCDA. The peak at 2.498 ppm corresponds to the chemical shift of H in the DMSOd₆ solvent, while the peak at 3.346 ppm corresponds to the chemical shift of HOD in the DMSOd₆ solvent. The ¹³C NMR spectrum (Figure S2b) of NTCDA shows three peaks at 124.03 ppm, 127.78 ppm, and 131.03 ppm, corresponding to the three types of sp² carbons of the benzene ring structures, while the ¹³C NMR peak at 158.85 ppm corresponds to sp² carbons in the anhydride groups (O=C-O-C=O). The septet peak centered at

~38 ppm corresponds to ¹³C in the DMSOd₆ solvent.

Scheme 1. The chemical structure of the redox-active polymers (P3, P5, P7, P9, and P11) and the reaction mechanism in Mg RFBs.





The ¹H NMR spectrum (Figure S3a-S7a) of P3, P5, P7, P9, and P11 each shows a peak at ~8.6-8.7 ppm, representing the four protons of the benzene rings in the NTCDA moieties of the polymer. The peak at ~7.2 ppm corresponds to the chemical shift of H in the CDCl₃ solvent, while the barely visible peak at ~1.2 ppm corresponds to the chemical shift of HOD in the CDCl₃ solvent. The peaks at ~4.4 ppm and ~3.5–3.8 ppm correspond to the protons in the PEG chain. The ¹³C NMR spectra (Figure S3b-S7b) of P3, P5, P7, P9, and P11 show peaks at ~70.5 ppm, ~70.07 ppm, ~67.7 ppm, and ~39.5 corresponding to the sp³ carbons of the PEG chain. The triplet peak centered at ~77 ppm corresponds to the chemical shift of ¹³C in the CDCl₃ solvent. The two peaks at ~126 ppm and ~130.9 ppm correspond to two types of sp² carbons of the benzene rings in the NTCDA moieties of the polymers (P3, P5, P7, P9, and P11). Since the three sp² carbon peaks of NTCDA are close to each other in ¹³C NMR spectra, two peaks for sp² carbons in the NTCDA moieties of the polymers may be merged to show one peak at ~126 ppm. The peak at ~162 ppm corresponds to the sp² carbons in the imide groups (O=C-N-C=O). These characterization results confirm the molecular structures of the polymers (P3, P5, P7, P9, and P11).

To tune the solubility, the monomers based on a PEG moiety with different chain length were used for the poly-

Table 1. The solubility of polymers with different PEG chain length.		
Sample	Solubility (g/L)	
Р3	0.06	
P5	0.12	
P7	2	
P9	10	
P11	4	

condensation with NTCDA. The solubilities of the synthesized polymers (P3, P5, P7, P9 and P11) were measured and the result is summarized in Table 1. As shown in Table 1, P7, P9 and P11 are 1–2 order of magnitude more soluble than P3 and P5 in the electrolyte. Among them, P9 has the highest solubility, which is 10 g/L. This result confirmed our hypothesis that by introducing PEG moiety, the solubility of polymers can indeed be tuned. When the PEG chain length is less than nine, increasing the chain length results in higher solubility. However, when the PEG chain length is increased to 11, the solubility of polymer starts to decrease, which could be due to the higher molecular weight of the P11.

Electrochemical performance

To evaluate the electrochemical performance of the designed polymers at the molecular level, their cyclic voltammograms (CV) were collected. Figure 2a-2c shows the CV curves of saturated P3, P5 and P7 at a scan rate of 100 mV/s using a glass carbon as the working electrode and Mg foils as both the counter and reference electrodes. For P3 and P5, the cathodic peak potentials are 1.51 V and 1.55 V, and the anodic peak potentials are 1.77 V and 1.99 V. The peak separation (∠E_n) of P5 (0.44 V) is higher than that of P3 (0.26 V), indicating that P3 are more electrochemically reversible than P5. For P7, CV shows two cathodic peaks (1.58 V and 0.99 V) and two anodic peaks (2.53 V and 2.05 V). Because the solubility of P7 is one order of magnitude higher than those of P3 and P5, it can be inferred that with the increase of solubility, more redox active materials participate in the reaction involving multiple charge transfer. In Figure 2a-2c, two pairs of redox peaks were observed in P7, while one pair of broad peaks were observed for P3 and P5. The

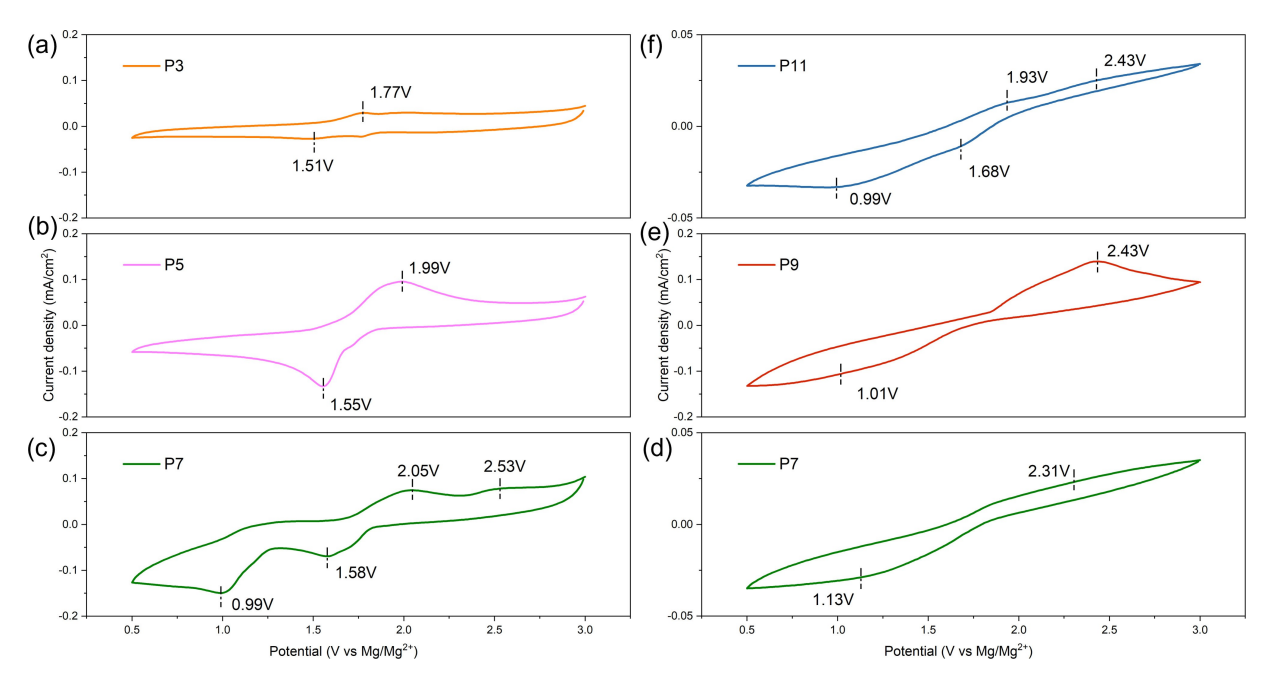


Figure 2. CV curves of saturated polymer catholytes at a scan rate of 100 mV/s at room temperature. For CV test of (a) P3, (b) P5 and (c) P7, a glass carbon was used as the working electrode. For CV test of (d) P7, (e) P9 and (f) P11, a carbon felt with known surface area was used as the working electrode.





different behaviors were caused by the overlap of redox peaks in P3 and P5 as evidenced by small bumps at ~1.7 V during the reduction. Due to the larger size of P9 and P11, CV curves of saturated P9 and P11 at the same scan rate show no detectable redox signals due to mass transfer limitation. To address this problem, carbon felt with known surface area was used as the working electrode, and CV curves (Figure 2d-2f) of saturated P7, P9 and P11 were collected at a scan rate of 100 mV/s. With the high-surface-area carbon felt, the two pairs of peaks of P7 become difficult to distinguish, and a cathodic peak at 1.13 V and an anodic peak at 2.31 V can be identified. Similar patterns were observed for CV curves of P9 and P11, albeit the two pairs become increasingly more distinguishable as the ether chain length increases. The peak current density of P9 is around four times higher than P7 and P11, which is likely due to its higher solubility.

Since high active material solubility is desired for RFBs, saturated P7, P9 and P11 were selected among all the synthesized polymers for additional electrochemical study. Their redox behaviors were examined by CV at different scan rates using a carbon felt as the working electrode. As shown in Figure 3a–3 c, the peak separations for three polymer solutions,

 ΔE_{p} , are above 1 V. The peak potentials, E_{p} , shifts to more extreme potentials with increasing scan rate. The peak currents exhibit a linear correlation with the square root of the scan rates (Figure 3d-3f). The standard rate constants (k⁰) are determined with this result using reported method. [24] Figure 3g-3i show linear fit between natural log of the peak reduction current versus the difference in potential between the voltage at the peak reduction current (Epa) and the calculated E₀ of the reduction. The diffusion coefficients of the polymers are obtained based on this result using a reported method. [24] To quantify the cross-over of the polymer molecules through the nanoporous membrane, permeability tests were performed as detailed in the experiment section. The obtained diffusion coefficients D₀, standard rate constant k⁰ and the permeability of the three polymers are listed in Table 2. The results suggest that the permeability slightly decreases with increasing the PEG chain length. However, the diffusion coefficient and reaction rate constant do not show a monotonic correlation with the PEG chain length. P9 shows the maximum diffusivity, and reaction rate constant. There are two factors, which can impact the solubility, diffusivity, and reaction rate constant of these polymers: 1) the PEG chain length; 2) the

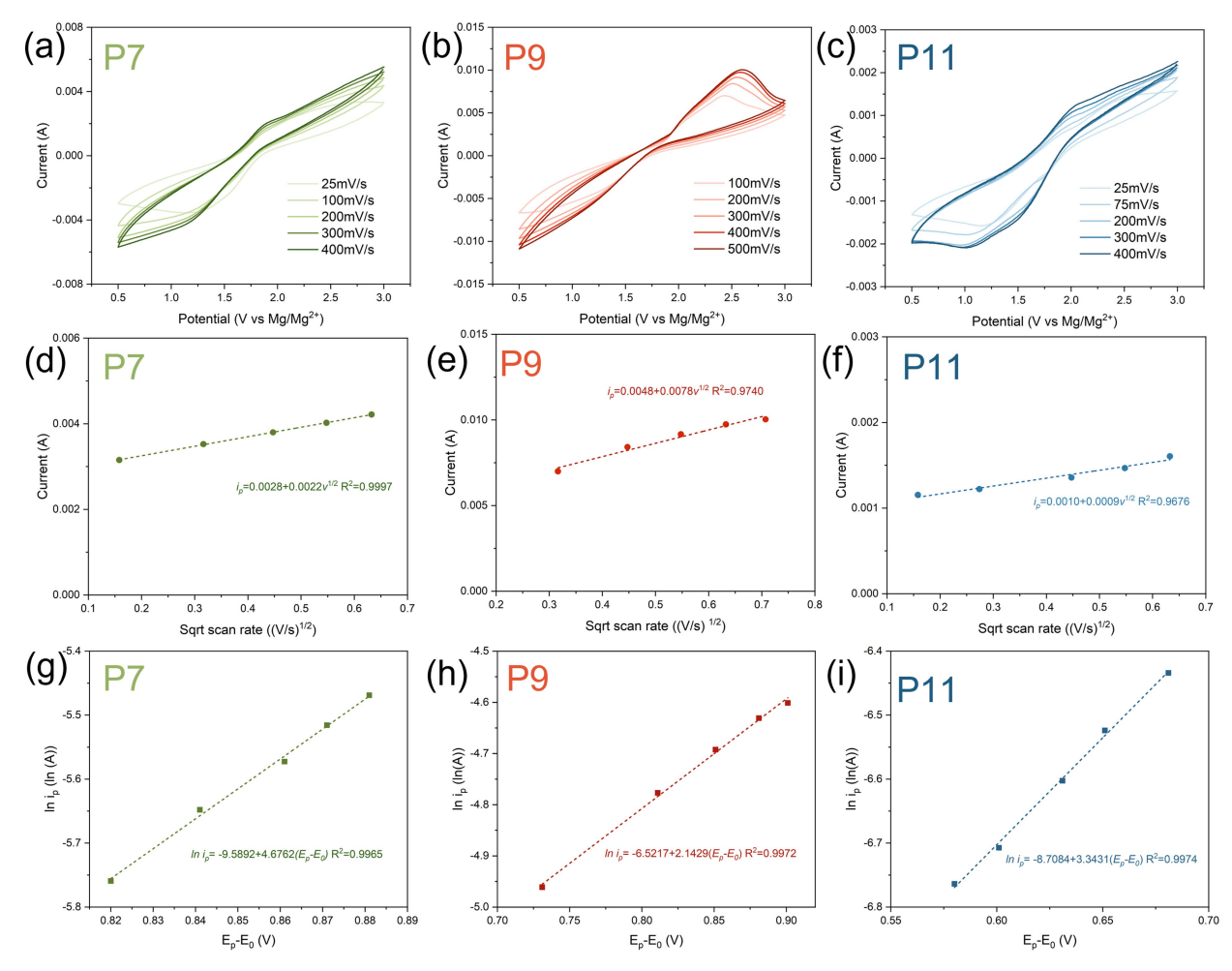


Figure 3. The cyclic voltammograms of saturated (a) P7, (b) P9 and (c) P11 obtained at different scan rates. Relationship between peak current and $v^{1/2}$ for cyclic voltammograms of (d) P7, (e) P9 and (f) P11. Relationship between the natural log of the peak reduction current (i_{pa}) and the difference in potential between the voltage at the peak reduction current (E_{pa}) and the calculated E_0 of the reduction for saturated (g) P7, (h) P9 and (i) P11.





Table 2. Properties of the synthesized polymers.				
Polymer	$D_0 (10^{-8} \text{ cm} \cdot \text{s}^{-1})$	$k^{0}(10^{-4} \text{ cm} \cdot \text{s}^{-1})$	Permeability ($\% \cdot day^{-1}$)	
P7	1.0	0.4	9.72	
P9	4.1	5.2	9.27	
P11	0.3	1.4	8.20	

polymer molecular weight. The best reaction kinetics of P9 may be due to its proper molecular weight for the redox reaction in Mg RFBs compared to P7 and P11. It can be concluded based on these results that P9 owns the highest solubility, highest diffusion behavior, and highest reaction rate.

Flow battery performance

Next, we examine the electrochemical performance of the synthesized polymers at the device level with a home-made flow cell (Figure 1). The typical CV curves of the electrolyte and polymer catholyte are shown in Figure S8, which demonstrate the feasibility of realizing a flow cell with 1.8 V. RFBs using Mg foils as the anode, a nanoporous membrane as the separator, and saturated polymer catholytes were assembled and galvanostatically discharged/charged. As shown in Figure 4a, the capacity increases as the PEG chain length increases up to P9, who can deliver a discharge capacity of 475 mAh/L. However, the capacity starts to decrease beyond P9, as P11 can only deliver 250 mAh/L. The discharge capacity shows a linear dependence on the polymer's solubility (Figure 4b), indicating the capacity is mainly governed by the polymer's concentration. To exclude the concentration effect and evaluate how the

physio-chemical properties of the polymer affect the performance of the RFBs, Mg RFBs with polymer catholytes containing the same concentration of P7, P9 and P11 (2 g/L) were assembled, and the same charge/discharge tests were performed. Cells with these three polymer catholytes deliver a discharge capacity of 84 mAh/L, 220 mAh/L and 135 mAh/L, respectively. The superior performance of P9 over other two polymers can be attributed to its highest reaction rate and diffusion coefficients.

The cycling performance of Mg RFBs with the synthesized polymer catholytes are shown in Figure 4c and Figure 4d. P3 and P5 show very stable cycling for 20 cycles (>94% capacity retention) and high Coulombic efficiency (CE) (>95%). In contrast, P7, P9 and P11 show much faster capacity fade. For P7 and P11, their capacity decreases to ~60% after 20 cycles. The CE of P7 decreases gradually from 93.0% in the first cycle to 70.2% at the 18th cycles, whereas the CE of P11 slightly increases from 94.3% to 98.2% during cycling. P9 experiences the fastest capacity fading among all the synthesized polymers (21.7% retention at 20th cycle), while showing an increasing CE from 82.0% to 96.0% during cycling. Given these polymers have similar permeability, it is unlikely the different capacity fading rate is mainly due to cross-over of the polymer molecules. The better cycling stability of the polymers with short-chained ether moiety (P3 and P5) than others could be primarily attributed to their low capacity therefore less cycle time for the same cycle number. Similarly, the better cycling stability of P7 and P11 than P9 could also be primarily attributed to their low capacity thereby less cycle time. The worse CE of P7 than P11 is consistent with its highest cross-over (permeability) and its worse cycling stability than P11. Based on these results, the

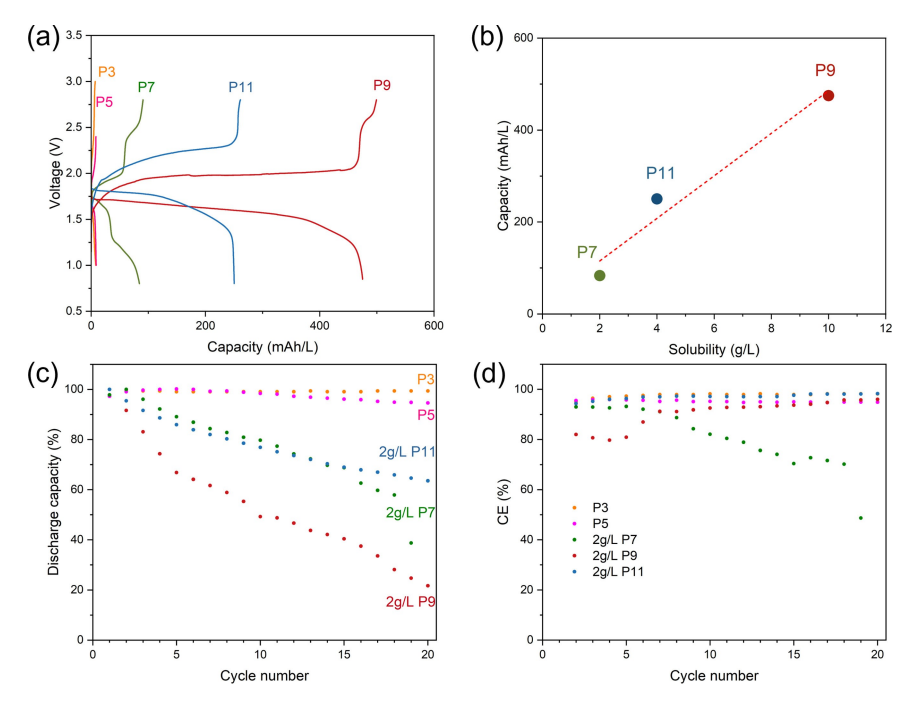


Figure 4. Flow battery performance of different polymers. (a) Charge/discharge voltage profiles of Mg RFBs with catholytes made from saturated polymer solutions of P3, P5, P7, P9 and P11. (b) Relationship between polymer solubility with its capacity. (c, d) Cycling performance and CE of the Mg RFBs with saturated P3, P5, and 2 g/L P7, P9 and P11.





cycling stability of the synthesized polymers is mainly governed by the total cycle time, whereas the cross-over plays a secondary role. This observation suggests the polymer molecules are likely not stable at its reduced states.

To optimize the cycling performance of Mg RFBs, it is necessary to identify the mechanisms of capacity decay, especially the main factor that causes the different behaviors of the polymers. In theory, three possible mechanisms can cause capacity loss during cycling: 1) loss of catholyte, 2) reactions between the cross-overed polymer molecules with the Mg anode, and 3) irreversible side reaction of the polymer molecules at their reduced states. Next, P9 is selected for a mechanistic study to understand capacity fading mechanisms given its fastest capacity loss.

In a typical flow battery test (~140 hours), roughly 20% catholyte volume was lost after cycling, despite of no obvious leakage sign. Therefore, the loss of catholyte volume could be due to the evaporation of DME solvent given its low boiling point and high vapor pressure. Since the capacity decay of P9 (78%) is much larger than the catholyte volume loss (20%), there must be other reasons to account for the capacity decay except for the cell leakage. To further investigate the mechanism, the cycled P9 catholyte was tested with CV, and the curve (Figure 5a) shows a similar redox behavior without no new peaks compared to the catholyte before cycling, while the peak current decreases by 72%. This result indicates that no new redox-active molecules are formed after cycling, but the concentration of P9 decreases remarkably. The FTIR of the electrolyte and P9 catholyte before and after cycling were collected and compared in Figure 5b. Compared with the electrolyte, P9 catholyte has apparent absorbance peaks between 1800 cm⁻¹ and 1500 cm⁻¹, corresponding to the vibration of carbonyl and benzene rings. There is no obvious difference between the FTIR profiles of P9 catholyte before and after cycling. This result indicates the cycling does not form any new soluble molecules in the catholyte solution, which is consistent with the CV result. The reduced P9 concentration and the absence of new molecules in the cycled catholyte suggest P9 undergoes side reactions during cycling and forms insoluble products.

To confirm the side reactions of P9, the cathode (graphite felt) and anode (Mg foil) after cycling were examined with

scanning electron microscopy (SEM) and energy dispersive spectroscopy (EDS). Although large polymers are designed to minimize the crossover through the non-ion selective porous separator, the permeability test (Table 2) demonstrates the polymer molecules still have considerable crossover (~ 9%·day⁻¹). For RFBs with a solid metal anode and only one electrolyte stream (as in our case), active material cross-over does not necessarily cause capacity fade, because the cross-overed molecules can still go back to the cathode chamber and be able to undergo redox reaction. Capacity fade will happen, however, if the cross-overed molecules undergo irreversible reactions with the Mg anode and leave the electrolyte. Cycled Mg foil was washed with DME to remove any soluble precipitate and examined with SEM. As shown in Figure 6a, the Mg foil anode undergoes obvious changes after cycling. SEM images (Figure 6b and Figure 6c) show a film formed on the surface of the Mg foil anode. Comparing the EDS (Figure 6d) of spot A (the formed film) and spot B (the crack that exposes the underneath Mg foil), the film contains much higher amount of C element and less amount of Mg element (45.3% of C element and 35.1% of Mg element) than the exposed Mg foil under the film, suggesting the cross-overed polymer reacts with the Mg foil anode and forms some insoluble product.

In addition to reacting with the Mg foil anode, the polymer molecules may undergo irreversible side reactions at its reduced state (the as-synthesized polymer is in its oxidized state), which is a common issue for organic materials for flow batteries. [25] To verify the stability of the polymer catholyte at its reduced state, the cell was discharged to 0.8 V first and then put into rest. After the 12-hour rest, the test was resumed. The discharge capacities before and after the rest are compared (Figure S9). The result shows that the cell loses 9.10% of the discharge capacity after resting at the discharged state, which is much higher than the typical capacity loss per cycle during a normal cycling without long rest (3.92%). Optical image (Figure 6e and Figure 6f) of the recovered carbon felt from the cycled flow cell shows the presence of some yellow solid particles in the graphite felt, and the SEM images (Figure 6q-6i) show there are lots of substance covering the individual fibers of the carbon felt comparing with the pristine carbon felt (Figure 6j). EDS of the solid precipitate (Figure 6k) demonstrates it contains large amount of C element and O element,

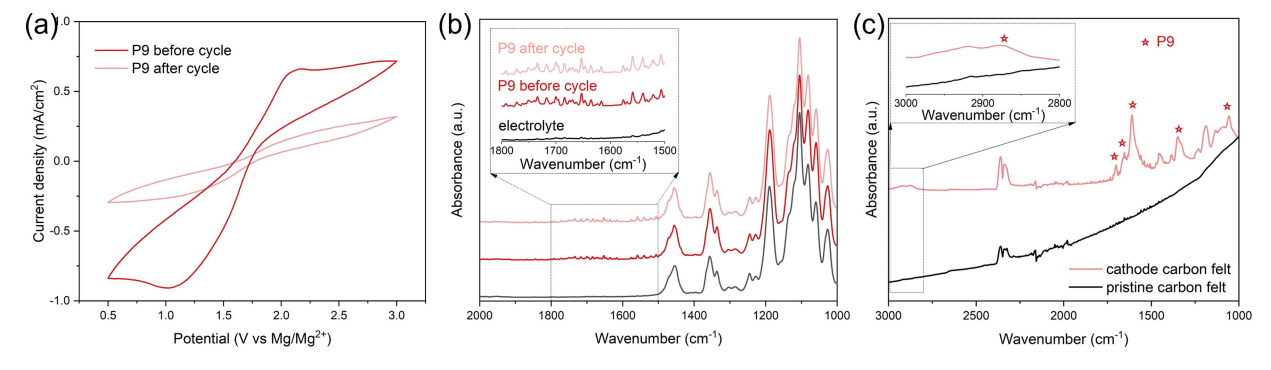


Figure 5. (a) CV curves of 2 g/L P9 catholyte before and after 20 cycles. (b) FTIR spectra of the electrolyte and 2 g/L P9 catholyte before and after 20 cycles. (c) FTIR spectra of pristine carbon felt and cathode carbon felt recovered from cells after 20 cycles.





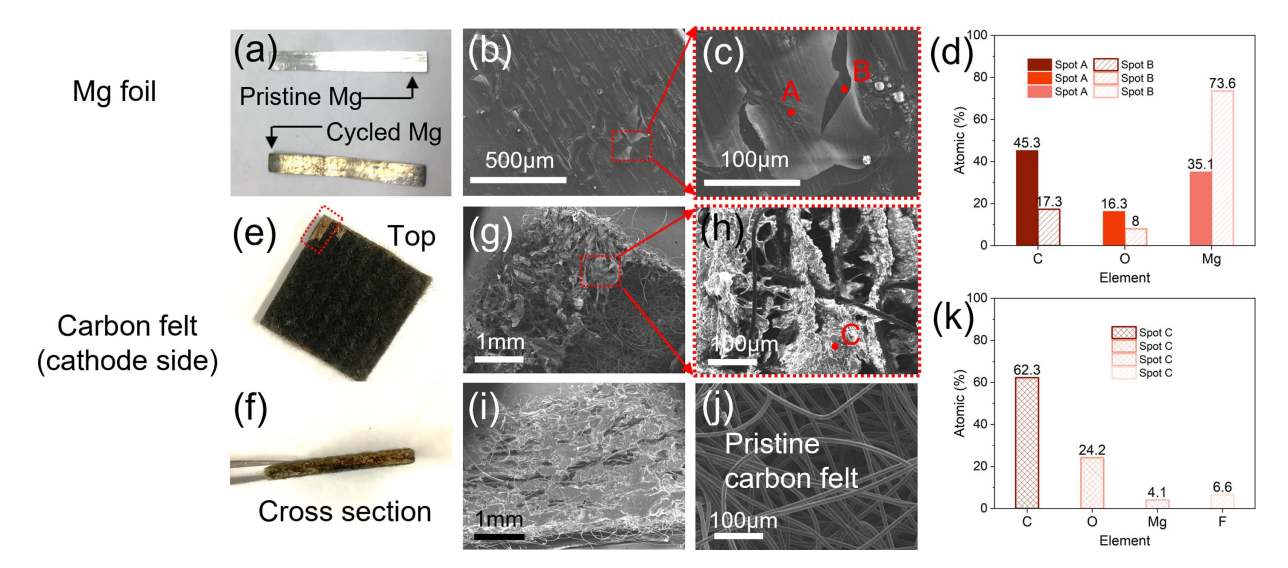


Figure 6. Optical image of recovered (a) Mg foil anode, (e) (f)carbon felt cathode. SEM image of recovered (b) (c) Mg foil anode, (g-i) carbon felt cathode, and (j) pristine carbon felt. EDS analysis of the recovered (d) Mg foil anode and (k) carbon felt cathode.

suggesting the polymer molecules at the reduced states precipitated from the catholyte due to irreversible chemical reaction. FTIR spectra (Figure 5c) of pristine carbon felt and cathode carbon felt after cycles were also collected. Compared with the pristine carbon felt, the cycled carbon felt has obvious peaks between 1800 cm⁻¹ and 1000 cm⁻¹ that correspond to the polymers. This result confirms that insoluble organic compound forms from the irreversible chemical reaction of the polymers.

Conclusion

In summary, through rational molecular engineering, polymer catholytes using NTCDA as the redox-active moiety and PEG chain as the supporting moiety for tuning the solubility are designed and synthesized. The correlation between the supporting moiety chain length and the performance of the carbonyl-based polymer catholyte in non-aqueous Mg hybrid flow batteries was systematically studied. The PEG chain length affects the solubility, redox kinetics, diffusivity, permeability, as well as the stability of the polymer catholyte. The solubility, redox kinetics and diffusivity of the polymer molecules show strong dependence on PEG chain length, and best solubility, highest reaction constant and fast diffusivity was achieved for polymer with PEG chain length x=9, whereas the permeability of the polymer molecules through a nano-porous membrane only slightly decreases with the PEG chain length. Cycling tests shows the polymer with PEG chain length x=9 shows the fast capacity loss, which is mainly attributed to its instability at discharged state. These fundamental insights will enable future molecular design and optimization to fully unleash the potential of non-aqueous Mg RFBs. Broadly, the knowledge in the synthesis and electrochemistry of the carbonyl-based redoxmer is beneficial to other applications of redox-active polymers, such as aqueous redox flow battery, organic material battery, electrochemical sensors, CO₂ capture, etc.

Acknowledgment

T.G. acknowledges University of Utah for providing the start-up funding. C.L. acknowledges the US National Science Foundation Award No. 2000102.

Conflict of Interest

The authors declare no conflict of interest.

Keywords: carbonyl polymer \cdot flow battery \cdot magnesium anode \cdot non-aqueous electrolyte \cdot porous membrane

- K. Lin, Q. Chen, M. R. Gerhardt, L. Tong, S. B. Kim, L. Eisenach, A. W. Valle,
 D. Hardee, R. G. Gordon, M. J. Aziz, M. P. Marshak, *Science* (80-). 2015,
 349 (6255), 1529–1532. https://doi.org/10.1126/science.aab3033.
- [2] H. Chen, G. Cong, Y. C. Lu, J. Energy Chem. 2018, 27 (5), 1304–1325. https://doi.org/10.1016/j.jechem.2018.02.009.
- [3] P. Leung, A. A. Shah, L. Sanz, C. Flox, J. R. Morante, Q. Xu, M. R. Mohamed, C. Ponce de León, F. C. Walsh, J. Power Sources 2017, 360, 243–283. https://doi.org/10.1016/j.jpowsour.2017.05.057.
- [4] O. R. Luca, J. L. Gustafson, S. M. Maddox, A. Q. Fenwick, D. C. Smith, Org. Chem. Front. 2015, 2 (7), 823–848. https://doi.org/10.1039/c5qo00075k.
- [5] K. Gong, Q. Fang, S. Gu, S. F. Y. Li, Y. Yan, Energy Environ. Sci. 2015, 8 (12), 3515–3530. https://doi.org/10.1039/c5ee02341f.
- [6] R. M. Darling, K. G. Gallagher, J. A. Kowalski, S. Ha, F. R. Brushett, Energy Environ. Sci. 2014, 7 (11), 3459–3477. https://doi.org/10.1039/ c4ee02158d.
- [7] Y. Huang, S. Gu, Y. Yan, S. F. Y. Li, Curr. Opin. Chem. Eng. 2015, 8, 105–113. https://doi.org/10.1016/i.coche.2015.04.001.
- [8] Y. Yan, S. G. Robinson, M. S. Sigman, M. S. Sanford, J. Am. Chem. Soc. 2019, 141 (38), 15301–15306. https://doi.org/10.1021/jacs.9b07345.
- [9] N. H. Attanayake, J. A. Kowalski, K. V. Greco, M. D. Casselman, J. D. Milshtein, S. J. Chapman, S. R. Parkin, F. R. Brushett, S. A. Odom, Chem. Mater. 2019, 31, 4363. https://doi.org/10.1021/acs.chemmater.8b04770.





- [10] J. Chai, A. Lashgari, Z. Cao, C. K. Williams, X. Wang, J. Dong, J. Jiang, ACS Appl. Mater. Interfaces 2020, 12 (13), 15262–15270. https://doi.org/10.1021/ACSAMI.0C01045/SUPPL(((AMP)))lowbar(((SEMI)))FILE/AM0C01045(((AMP)))lowbar(((SEMI)))SI(((AMP)))lowbar(((SEMI)))001.PDF.
- [11] M. J. Baran, M. N. Braten, E. C. Montoto, Z. T. Gossage, L. Ma, E. C. Chénard, J. S. Moore, J. Rodríguez-Lópezlópez, B. A. Helms, *Chem. Mater.* 2018, 30, 30. https://doi.org/10.1021/acs.chemmater.8b01318.
- [12] J. Winsberg, S. Benndorf, A. Wild, M. D. Hager, U. S. Schubert, J. Winsberg, S. Benndorf, M. D. Hager, U. S. Schubert, A. Wild, *Macromol. Chem. Phys.* **2018**, *219*, 17700267. https://doi.org/10.1002/macp. 201700267.
- [13] X. Fang, Z. Li, Y. Zhao, D. Yue, L. Zhang, X. Wei, ACS Mater. Lett. 2022, 4, 277–306. https://doi.org/10.1021/acsmaterialslett.1c00668.
- [14] J. Zhang, J. Huang, L. A. Robertson, R. S. Assary, I. A. Shkrob, L. Zhang, J. Phys. Chem. C. 2018, 122, 8116–8127. https://doi.org/10.1021/acs.jpcc. 8b01434.
- [15] M. Li, Z. Rhodes, J. R. Cabrera-Pardo Ab, S. D. Minteer, Sustain. Energy Fuels 2020, 4, 4370. https://doi.org/10.1039/d0se00800a.
- [16] N. H. Attanayake, Z. Liang, Y. Wang, A. P. Kaur, S. R. Parkin, J. K. Mobley, R. H. Ewoldt, J. Landon, S. A. Odom, *Mater. Adv.* 2021, 2 (4), 1390–1401. https://doi.org/10.1039/d0ma00881h.
- [17] Y. Yan, D. B. Vogt, T. P. Vaid, M. S. Sigman, M. S. Sanford, Angew. Chem. Int. Ed. 2021, 60, 27039–27045. https://doi.org/10.1002/anie.202111939.
- [18] J. A. Kowalski, L. Su, J. D. Milshtein, F. R. Brushett, Curr. Opin. Chem. Eng. 2016, 13, 45–52. https://doi.org/10.1016/j.coche.2016.08.002.

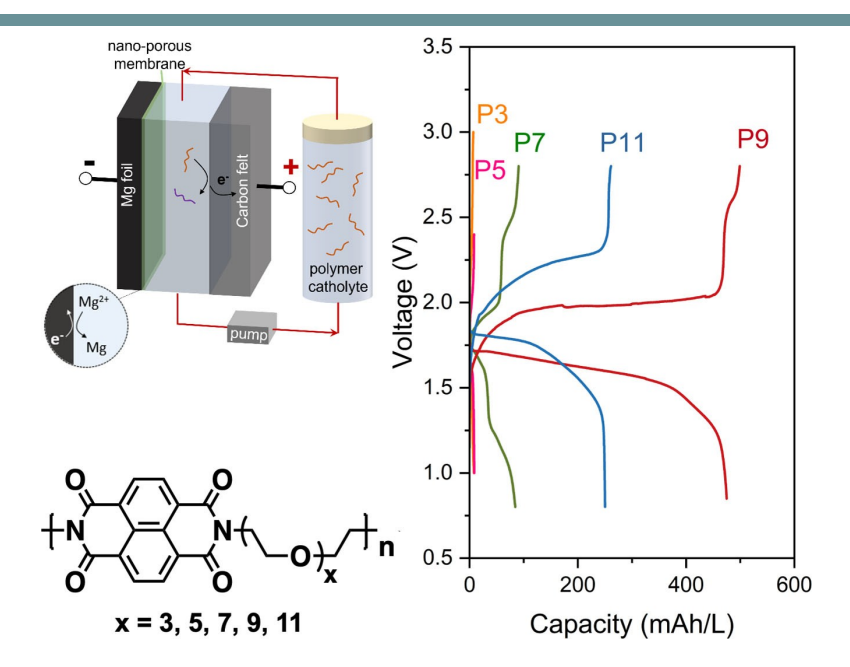
- [19] X. Wei, W. Xu, M. Vijayakumar, L. Cosimbescu, T. Liu, V. Sprenkle, W. Wang, Adv. Mater. 2014, 26 (45), 7649–7653. https://doi.org/10.1002/adma.201403746.
- [20] Y. Zhao, Y. Ding, Y. Li, L. Peng, H. R. Byon, J. B. Goodenough, G. A. Yu, Chem. Soc. Rev. 2015, 44 (22), 7968–7996. https://doi.org/10.1039/ c5cs00289c.
- [21] M. Park, J. Ryu, W. Wang, J. Cho, Nat. Rev. Mater. 2016, 2 (1). https://doi. org/10.1038/natrevmats.2016.80.
- [22] H. D. Yoo, I. Shterenberg, Y. Gofer, G. Gershinsky, N. Pour, D. Aurbach, Energy Environ. Sci. 2013, 6 (8), 2265–2279. https://doi.org/10.1039/ c3ee40871j.
- [23] Y. Qin, K. Holguin, D. Fehlau, C. Luo, T. Gao, ACS Appl. Energ. Mater. 2022, 5, 2675–2678. https://doi.org/10.1021/acsaem.2c00363.
- [24] H. Wang, Y. S. Sayed, E. J. Luber, B. C. Olsen, S. M. Shirurkar, S. Venkatakrishnan, U. M. Tefashe, A. K. Farquhar, E. S. Smotkin, R. L. Mccreery, J. M. Buriak, ACS Nano 2020, 14. https://doi.org/10.1021/acsnano.0c01281.
- [25] J. Luo, B. Hu, M. Hu, Y. Zhao, T. L. Liu, ACS Energy Lett. 2019, 4 (9), 2220–2240. https://doi.org/10.1021/acsenergylett.9b01332.

Manuscript received: June 3, 2022
Revised manuscript received: August 21, 2022
Accepted manuscript online: August 22, 2022
Version of record online:



CHEMISTRY AN ASIAN JOURNAL Research Article

RESEARCH ARTICLE



Y. Qin, K. Holguin, D. Fehlau, C. Luo*, T. Gao*

1 – 10

Exploring Carbonyl Chemistry in Non-aqueous Mg Flow Batteries



This work reports a non-aqueous Mg flow battery which integrates a Mg foil anode, a porous membrane with a polymer solution catholyte. Through rational molecular engineering, carbonyl group was used as redox-

active moiety and a polyethylene glycol chain was used to tune the solubility. The Mg flow battery can deliver a voltage of 1.8 V and a capacity of ~500 mAh/L.